PAPER

Check for updates

Effects of pyrolysis temperature on plant-seed-derived carbon dots

Ken Inoue, [ID] [a] Ryo Suzuki, [ID] [a] Yuko Kaneda, [b] Makoto Tanimura, [b] Kazuteru Shinozaki [ID] [a] and Masaru Tachibana [ID] *[a]

Carbon dots (CDs) from natural sources can be produced through pyrolysis, a simple, solvent-free, and cost-effective method suitable for large-scale production. However, there is limited research on the optimal pyrolysis conditions for synthesizing natural CDs with fluorescent properties. Understanding how synthesis conditions impact the optical and structural characteristics is crucial for enhancing the fluorescence of natural CDs. This study investigates the structures and optical properties of natural CDs synthesized from plant seeds at different pyrolysis temperatures. Effective synthesis of fluorescent CDs was observed at temperatures corresponding to mass reduction. Higher pyrolysis temperatures enhanced the carbon core's crystallinity, leading to a quantum yield increase to approximately 30%, comparable to CDs synthesized using conventional methods. These findings offer valuable insights into producing fluorescent CDs from natural sources.

Introduction

Carbon dots (CDs) are carbon-based semiconductor crystals with diameters of 10 nm or less.[1] Discovered in 2004 by Xu *et al.* during the production of single-layer carbon nanotubes,[2] various types of CDs with superior fluorescence properties have since been reported.[3] In contrast to traditional inorganic quantum dots derived from materials such as cadmium, CDs are valued for their low toxicity, biocompatibility, and ease of functionalization.[4,5] The unique features of CDs, such as their carbon core and surface layer exhibiting a core–shell structure,[6] position them as promising materials for applications in display, bioimaging, catalysis, and energy conversion.[7] The carbon core of a CD comprises crystalline or amorphous regions of sp^2/sp^3 carbon, while the surface layer is amorphous and contains functional groups based on oxygen or nitrogen.[8]

CDs have been successfully synthesized from chemical carbon sources such as graphite,[9] citric acid,[10,11] and phenylenediamine.[12,13] Meanwhile, in recent years, CDs derived from natural sources have garnered attention owing to their environmental friendliness and cost-effectiveness.[14] To fully leverage these benefits in practical applications, CDs need to demonstrate a high quantum yield (QY) and narrow full width at half-maximum (FWHM), which are crucial indicators of their luminescent properties. QY quantifies the capacity of a particle to emit absorbed

electromagnetic radiation as photons for fluorescent materials.[15] FWHM is critical for assessing the color purity of fluorescent materials.[16] However, achieving both high QY and a narrow FWHM typically necessitates extended synthesis durations, the utilization of hazardous solvents, and intricate purification techniques such as column chromatography.[17–19]

Natural CDs can be synthesized using techniques such as pyrolysis, hydrothermal treatment, and microwave irradiation, all of which facilitate carbonization and formation of CDs. Particularly, pyrolysis for CD synthesis is straightforward, involving only carbonization by heating. In contrast to hydrothermal or microwave methods, it does not require complex equipment, making it well-suited for large-scale production of CDs and enhancing its industrial viability.[20,21] Despite these advantages, limited research exists on how the pyrolysis temperature impacts the structural and optical characteristics (*e.g.*, QY and FWHM) of natural CDs. Although some studies have reported the dependence of pyrolysis temperature on CDs derived from natural precursors,[22–25] they have mostly focused on demonstrating the feasibility of using new natural sources or on specific applications, rather than systematically correlating synthesis conditions with key optical properties. Consequently, the correlation between pyrolysis parameters and fluorescence properties remains poorly understood. Therefore, there is a necessity to optimize the synthesis conditions and gain a comprehensive insight into the fluorescence mechanisms to further improve the fluorescence attributes of natural CDs.

Fenugreek seeds serve as a promising natural precursor for the synthesis of CDs exhibiting high crystallinity, reproducible PL properties, and excellent photostability.[26,27] Moreover, seeds

[a] *Department of Materials System Science, Yokohama City University, 22-2 Seto, Kanazawa-ku, Yokohama 236-0027, Japan. E-mail: tachiban@yokohama-cu.ac.jp*
[b] *Instrumental Analysis Center, Yokohama National University, 79-5 Tokiwadai, Hodogaya-ku, Yokohama 240 8501, Japan*

22832 | *J. Mater. Chem. C*, 2025, **13**, 22832–22840

This journal is © The Royal Society of Chemistry 2025

in general, in contrast to other natural precursors such as fruits, vegetables, flowers, and leaves, are not restricted by regional availability and possess superior durability, making them a sustainable starting material.

In this study, fenugreek-seed-induced CDs were synthesized under various pyrolysis temperature conditions with short synthesis times, specifically 40 min, and their fluorescence properties were evaluated.

Experimental methods

Synthesis of natural CDs

The synthesis of plant-seed-induced CDs is schematically illustrated in Fig. 1(a). CDs were produced through pyrolysis with fenugreek seeds serving as the carbon source (precursor).

The pyrolysis parameters were modified from the prior investigation (350 °C, 3 h).[27] Ethanol was selected as the extraction solvent for its compatibility with LED devices.[27] First, 5 g of powdered ground fenugreek-seed was placed in two crucibles (total of 10 g of fenugreek seeds) and heated in an electric furnace at 300, 350, 400, 440, 460, 480, 520, 560 °C for 40 min in air. The crucible containing the carbonized powder was removed from the furnace immediately after 40 min and cooled to room temperature (25 °C). Failure to remove it promptly would result in further sublimation, causing product loss; therefore, this step is essential. Subsequently, the carbonized powder was dispersed in 60 or 20 mL (only for CDs-520 and 560 since the extract concentration was low) of ethanol by sonication for 10 min. The resulting black mixture was then centrifuged at 15 000 rpm for 12 min to eliminate undissolved particles, and the supernatant was filtered using a filter with a pore size of 0.1 μm

(PALL ACRO DISC, Japan or GL Science Inc, Japan). CDs prepared at each temperature are denoted as "CDs-X," where X represents the pyrolysis temperature.

Structural characterization

The pyrolysis process of fenugreek seeds was examined by thermogravimetric analysis (TGA) (STA7300, HITACHI) at a heating rate of 15 °C min^{-1} under atmospheric conditions. The shape and structure of obtained CDs were observed by transmission electron microscopy (TEM) (JEM-2100F, JEOL) at 200 kV, where TEM grid underwent a hydrophilic treatment prior to sample placement, and the sample was dried immediately before imaging. The degree of graphitization of the CDs was evaluated using a laser Raman spectrometer (NRS-4500, JASCO) with an excitation wavelength of 532 nm, where the samples were prepared by drying the CD solutions using a mantle heater, and the resulting solids were placed on microscope slides for Raman measurements. The composition of the CDs was analyzed using a Fourier-transform infrared (FTIR) spectrometer (FT/IR-4100, JASCO) that featured an attenuated total reflection prism (ATR PRO ONE, JASCO), where the CD solutions were evaporated using the mantle heater, and the resulting solids were gathered for FTIR measurements.

Optical characterization

Photoluminescence (PL) spectra of the CD solutions were analyzed using a fluorescence spectrophotometer (FP-6500, JASCO). The absolute QYs were measured on a JASCO FP-8500 fluorometer with a 120-mm integrating sphere (ILF-135). Ultraviolet-visible (UV-vis) spectra of the CD solutions were obtained through UV-vis absorption spectroscopy (V-530, JASCO).
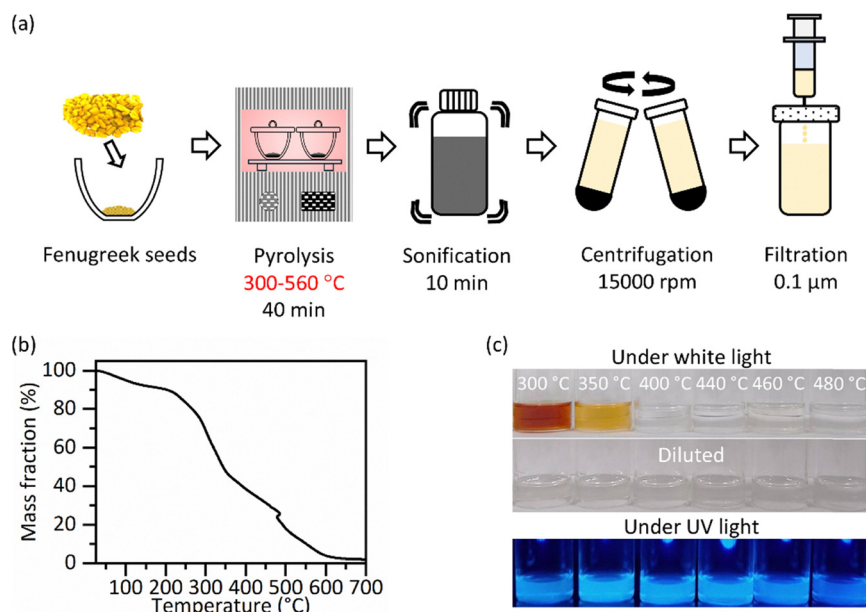

Fig. 1 (a) Schematic of the synthesis of CDs derived from fenugreek seeds through pyrolysis in air using an electric furnace. (b) TGA curve of fenugreek-seed powder. (c) Photographs of CDs dispersed in ethanol solutions.

Results and discussion

Structural analysis

TGA was conducted on fenugreek seed powder in air to examine the temperature-dependent mass loss. Fig. 1(b) shows the TGA profile of the fenugreek seed powder. Changes in slope observed between 300–350 and 400–480 °C is discussed later. To optimize the synthesis temperature, CDs were pyrolyzed at temperatures ranging from 300 °C to 560 °C, aligning with the decomposition temperature range of fenugreek seed powder, and the heating duration was also optimized, with 40 min being found to be the most suitable. Subsequently, the CDs synthesized at varying temperatures were extracted using ethanol. Fig. 1(c) and Fig. S1 display the CDs prepared in ethanol under daylight and UV light conditions. Notably, no clear fluorescence is observed in solutions prepared at decomposition temperatures above 520 °C, likely due to significant mass loss, as shown in Fig. 1(b). Conversely, the remaining solutions demonstrate distinct emissions under UV light, as shown in Fig. 1(c). This study focuses on investigating solutions displaying prominent light emission.

The production yields of CDs obtained from fenugreek seeds are less than 2.0%, which is similar to those of previously reported natural precursor-derived CDs.[28,29] Moreover, the yield is significantly low compared with those from common chemical sources such as citric acid[30] and phenylenediamine.[31] Generally, the production yields for natural precursor-derived CDs are low compared with those produced from common chemical sources, although only a limited number of reports have mentioned the production yields so far. Therefore, improving the production yield for natural precursor-derived CDs is one of the most critical challenges for practical applications and requires future studies.

The daylight-exposed solutions displayed diverse colors, possibly because of differences in concentrations of CDs and other soluble compositions. To assess the optical characteristics of CDs synthesized at varying temperatures, CD concentrations in the solutions were modified according to their UV-vis absorption spectra. The concentration was standardized with the optical absorption intensity at 260 nm, corresponding to the $\pi–\pi^{*}$ transition of the synthesized CDs. As shown in Fig. 1(c), all solution samples appear transparent. These concentration-normalized solution samples were analyzed in this investigation. The exact effect of other soluble components besides CDs such as residual carbon matter on PL and UV-vis spectrum is not well understood; however, even at significantly low CD concentration, no considerable impact is observed on spectral characterizations (PL and UV-vis) suggesting the negligible effect of other soluble components.

Bright-field images were acquired using TEM to verify the presence of CD particles. The bright-field images, high-resolution images, and the size distributions of CDs-300, 400, and 480 are shown in Fig. 2(a)–(c). Distinct CD particles are observed at each synthesis temperature. The particle size for CDs-300 is 6.5 ± 3.0 nm, for CDs-400 was 3.3 ± 1.2 nm, and for CDs-480 was 3.1 ± 1.1 nm. As shown in Fig. 2(d), CDs-300 exhibit a larger and more heterogenous size; however, an increase in the pyrolysis temperature results in a decrease in particle size and a uniform distribution. The smaller diameters of CDs-400 and CDs-480 may be attributed to the disintegration of surface functional groups at higher temperatures.

In the insets of high-resolution images shown in Fig. 2(a)–(c) and Fig. S2(a)–(c), particles exhibiting lattice fringes are observed. The proportion of observed lattice fringes is approximately 10% of the total particle count for CDs-300, whereas
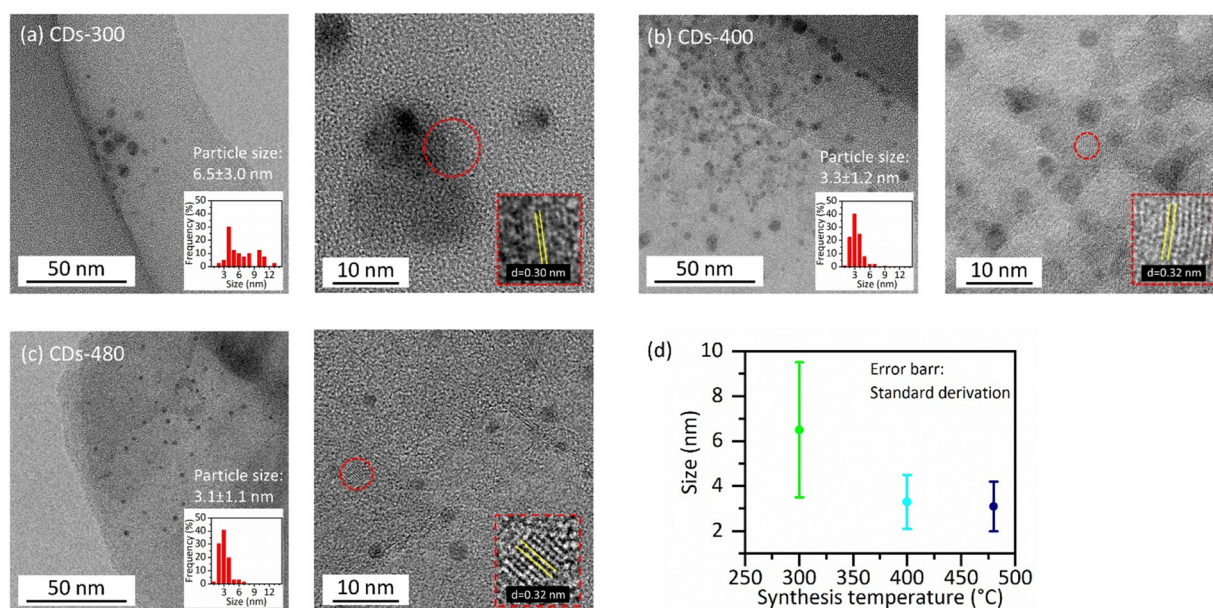

Fig. 2 Bright-field images (left), high-resolution images (right), size distributions (inset in bright-field images), and high-resolution lattice images (inset of high-resolution images) of (a) CDs-300, (b) CDs-400, and (c) CDs-480. The difference in particle contrast is because of diffraction contrast, which originates from differences in crystal orientation. (d) Size of CDs at each synthesis temperature.

22834 | *J. Mater. Chem. C*, 2025, **13**, 22832–22840

This journal is © The Royal Society of Chemistry 2025

CDs-400 and CDs-480 each represent approximately 40% of the total count. Most lattice fringes display an observed lattice spacing of 0.30–0.32 nm, corresponding to the (002) plane of graphite.[32–34] These findings indicate that the crystallinity, specifically the degree of graphitization, is higher in CDs-400 and CDs-480 compared with CDs-300. Additionally, some lattice spacing of 0.26–0.28 nm is noted, a value previously reported in studies on synthesized carbon dots, although it cannot be definitively linked to graphite lattice spacing. This lattice spacing may be associated with the precursor of graphitic CDs.

The Raman spectra of CDs-300, CDs-400, and CDs-480 are depicted in Fig. 3(a), showing the distinct D and G bands characteristic of carbon materials. These spectra were analyzed using the Voigt function, as shown in Fig. 3(b)–(d). For instance, the peak positions of the D and G bands in CDs-480 are found to be 1374 cm^{-1} and 1595 cm^{-1}, respectively. The peak intensity ratio (I_D/I_G), which is a critical parameter for estimating the crystallinity of carbon materials, is plotted in Fig. 3(e). As shown in Fig. 3(e), the I_D/I_G ratio decreases with increasing synthesis temperature, indicating an improvement in the crystallinity of the CDs.

For the compositional analysis of the CDs, FTIR spectra were obtained, as shown in Fig. 3(f). The FTIR analysis verifies that CDs synthesized at temperatures up to 480 °C exhibit common peaks, such as broad or shoulder peaks at 1340–1350 cm^{-1} (C–N), 1410 cm^{-1} (C–C), 1560 cm^{-1} (C=O), 1650 cm^{-1} (C=C), and at 2853, 2923, and 2960 cm^{-1} corresponding to CH and CH$_2$ groups, along with a broad peak around 3400 cm^{-1} attributed to OH and NH functional groups. Notably, CDs-300 and 350 exhibit distinctive peaks at 1742 cm^{-1} (C=O) and 1457 cm^{-1} (CH$_2$), which are not present in other samples.

The change in slope (between 300–350 °C and 400–480 °C) observed in the TGA curve (refer to Fig. 1(b)) is attributed to the decrease in the intensities of C=O and CH$_2$ (at 1457 cm^{-1}) and CH, CH$_2$ (at 2853–2960 cm^{-1}) peaks. Overall, all CDs share a similar surface chemical composition. Moreover, the intensities of CH and CH$_2$ peaks (at 2853–2960 cm^{-1}) decrease significantly from 400 °C. The peak stems from the carbon source (fenugreek seeds), and its reduction indicates increased carbonization,[35] enhancing CD crystallinity. This finding aligns with the particle size reduction observed in TEM and the increased crystallinity revealed by Raman spectra.

Optical analysis

Fig. 4(a) shows the UV-vis spectra (normalized at 245 nm) of CDs-300 to CDs-480. All samples exhibit similar UV-vis spectra with slightly varying peak intensities. The peak at around 260 nm in CDs-300 to CDs-480 corresponds to the π–π* transition of C=C bonds within the carbon core. The broad peak extending beyond 300 nm is associated with edge/surface transitions. A notable feature in the UV-vis spectrum is the π–π* transition. While the absorption band at 300 °C and 350 °C appears broad, it sharpens at 400 °C, indicating an enhancement in the crystallinity of the carbon core at this temperature. The PL spectra of CDs-300 to CDs-480, obtained with an excitation wavelength of 360 nm, are depicted in Fig. 4(b). These spectra display blue emission, with intensity rising as the synthesis temperature increases. Fig. 4(c) illustrates PL spectra normalized to the maximum intensity of each CD, indicating a slight shift towards shorter wavelengths with higher pyrolysis temperatures. Fig. 4(d) shows the emission peak position of the spectra of each CD. It is evident that the emission wavelength decreases almost linearly with
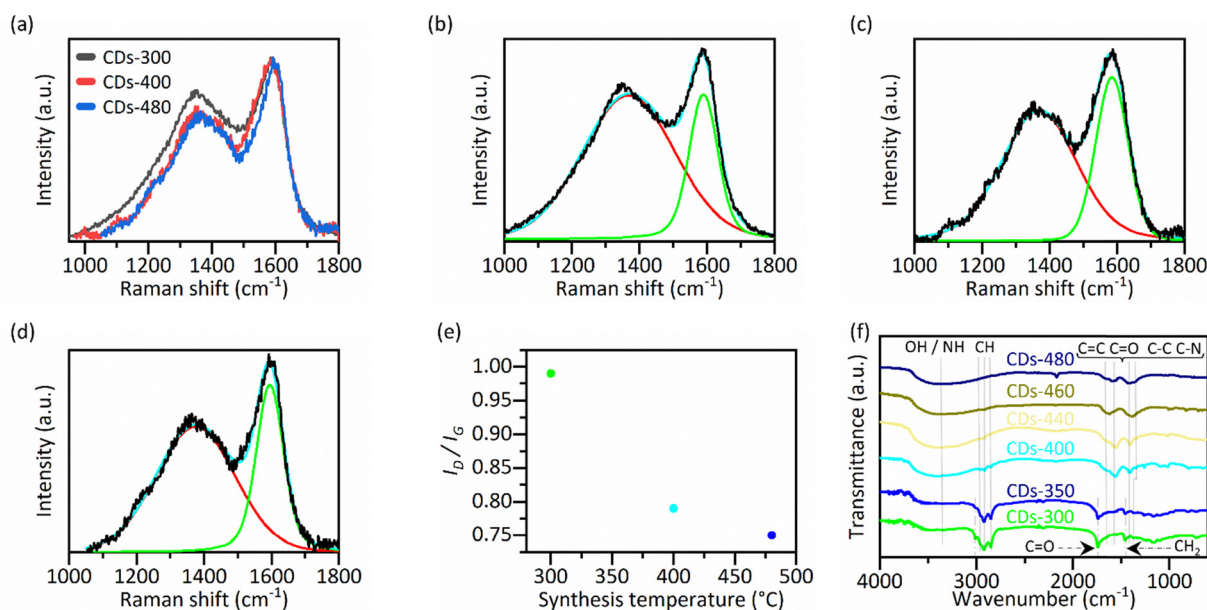

Fig. 3 (a) Raman spectra of CDs-300, 400, and 480. (b) Raman spectra of CDs-300, (c) CDs-400, and (d) CDs-480, fitted using the Voigt function. The black line represents the experimental data, the red and green lines represent the fitted curves, and the blue line indicates the sum of the fitted curves. (e) I_D/I_G of each CDs. (f) FTIR spectra of different CDs synthesized in this study.

This journal is © The Royal Society of Chemistry 2025

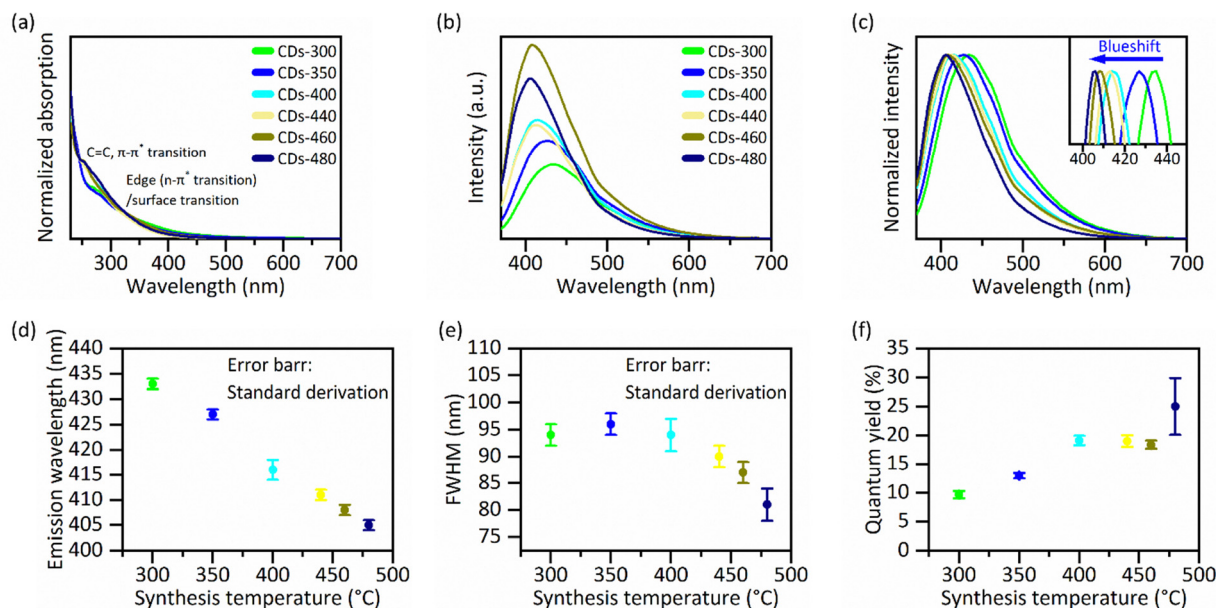*J. Mater. Chem. C*, 2025, **13**, 22832–22840 | **22835**

Fig. 4 (a) Normalized UV-vis spectra of all CDs (normalized at 245 nm). (b) PL spectra of CDs, taken at the excitation wavelength of 360 nm. (c) PL spectra normalized at the maximum intensity of each CD. (d) Average peak positions of CDs. (e) FWHM of the PL spectra of CDs taken under the excitation wavelength of 360 nm. (f) Average QYs of CDs measured under the excitation wavelength of 360 nm.

increasing temperature. This blue shift in emission wavelength is attributed to a decrease in defects as the synthesis temperature rises, resulting in a wider energy gap. It is worth mentioning that from the FTIR spectrum, the presence of C=O at 1742 cm^{-1} and CH$_2$ at 1457 cm^{-1} are observed only for CDs-300 and 350, with their peaks disappearing for CDs-400, suggesting potential changes in luminescence. However, no such changes in PL spectrum are observed. This indicates that the presence of C=O at 1742 cm^{-1} and CH$_2$ at 1457 cm^{-1} do not significantly affect the optical properties of CDs-300 and CDs-350.

Fig. 4(e) shows the FWHM of the PL spectra recorded under the excitation wavelength of 360 nm. The FWHM decreases with the temperature. The FWHM of the spectra is 94 nm for CDs-300, whereas it is 81 nm for CDs-480, indicating a decrease in FWHM by 13 nm at higher pyrolysis temperatures. The decrease in FWHM is attributed to the increased crystallinity of the CDs, which reduces defects and consequently narrows the FWHM. Fig. 4(f) shows the QYs of CDs measured at an excitation wavelength of 360 nm. The highest QY is 10.3% for CDs-300 and improves to 29.9% for CDs-480, which is nearly a threefold improvement, attaining a yield comparable to that of natural CDs synthesized *via* time-consuming and complex methods, as listed in Table S1.[28,36–63] This enhanced QY is also attributed to the increased crystallinity of CDs, as suggested by the Raman and UV-vis spectra. The QY data, Raman spectra, and FTIR peaks are summarized in Table S2 to provide a clearer understanding of the correlations between the optical and structural characteristics. It should be noted that, during the pyrolysis process in air, the oxidation of the precursor can introduce defects, which may induce non-radiative transitions and decrease the QY. However, as evident from the above discussion, as the heating temperature increases, CH groups,

one of the defects, are destroyed, leading to improved crystallinity and, consequently increased QY. Therefore, the optimization of pyrolysis conditions enhances the crystallinity of the CDs, thereby improving their fluorescence characteristics.

The pyrolysis method is a widely utilized bottom-up approach for synthesizing CDs, in which the precursor material breaks down into smaller carbon fragments.[64,65] As the temperature increases, these carbon fragments nucleate and grow into CDs. This approach helps to minimize the dependence on the type of precursor. Our results on the effect of temperature in CD synthesis by pyrolysis provide important insights into the synthesis from not only natural sources but also from chemical sources.

To study the PL mechanism, we analyzed the PL spectra of the CDs at various excitation wavelengths. Fig. 5(a)–(c) displays the normalized PL spectra for CDs-300, CDs-400, and CDs-480 at their respective emission peaks within the excitation wavelength range of 240–420 nm. The original PL spectra is provided in Fig. S3. These spectra exhibit two distinct components: a short-wavelength side "S" ($\sim$330 nm) and a long-wavelength side "L" (375 nm to 467 nm). The peak wavelength of the short-wavelength component "S" does not depend on the excitation wavelength and is constant. As shown in Fig. 6(a)–(c), the excitation spectra of the short-wavelength component exhibit a maximum at an excitation wavelength of $\sim$280 nm, corresponding to the π–π^* transitions of the aromatic clusters in the carbon core.[66] This observation indicates that the short-wavelength component is attributed to the emission from the π^* band edge (LUMO) associated with the π–π^* transitions in the carbon core. The relationship between the excitation wavelength and maximum peak wavelength of the longer-wavelength component is shown in Fig. 5(d). The peak
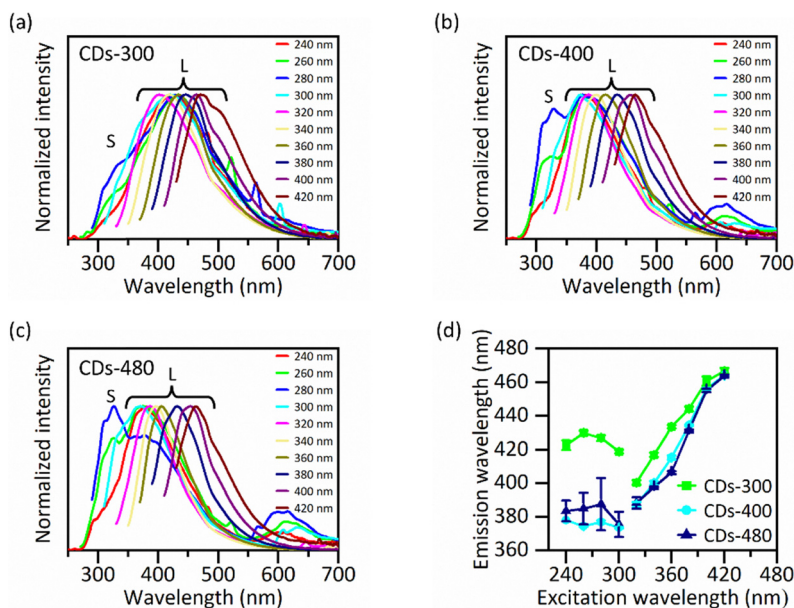
22836 | *J. Mater. Chem. C*, 2025, **13**, 22832–22840

This journal is © The Royal Society of Chemistry 2025

Fig. 5 PL spectra normalized at each excitation wavelengths' emission maximum of (a) CDs-300, (b) CDs-400, and (c) CDs-480. (d) Plots of long-wavelength emission peak "L" against the excitation wavelength for CDs-300, 400, and 480.
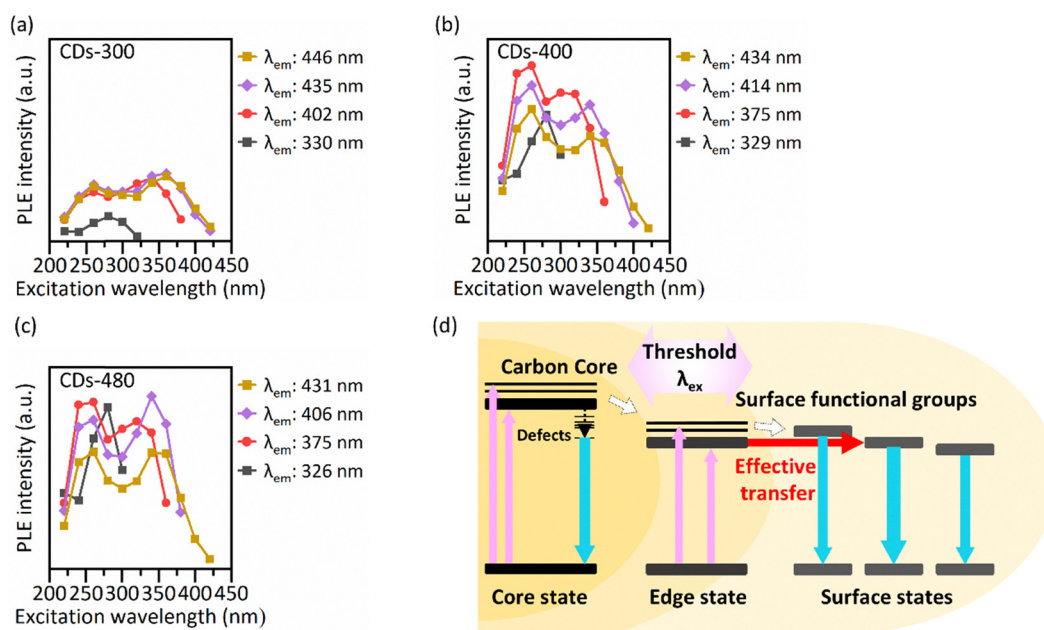

Fig. 6 Excitation spectra of (a) CDs-300, (b) CDs-400, and (c) CDs-480. (d) Schematic of the PL mechanism for the long-wavelength component.

wavelength of the long-wavelength component remains constant for excitation wavelengths below 300 nm, whereas it exhibits strong dependence on excitation wavelengths above 300 nm. This behavior, encompassing both excitation-dependent and excitation-independent PL, appears to be a prevalent characteristic in numerous CDs as previously documented.[66–70]

Previous studies[67,71] attribute the excitation independence of the long-wavelength component to emissions from defects within the carbon core, particularly evident at excitation

wavelengths below 300 nm where π–π^* transitions occur. Conversely, at longer excitation wavelengths surpassing 300 nm (threshold wavelength: λ_{th}), the absence of π–π^* transitions leads to excitation-dependent PL originating from edge states of the carbon core and surface states associated with surface functional groups situated within the π^* band (LUMO).[70] A schematic representation of the PL mechanism for the long-wavelength component is depicted in Fig. 6(d). The excitation spectra of the "excitation-dependent-long-wavelength"

component exhibit two maxima at around 260 nm and 360 nm, as shown in Fig. 6(a)–(c). These peaks are attributed to the π–π^* transitions of C=C and the n–π^* transitions of C=O, respectively.[69] Hence, the excitation dependence of the long-wavelength component arises from emissions linked to these transitions. The presence of two peaks in the excitation spectra further corroborates the assertion that edge/surface states are related to the π–π^* charge transfer transitions and the n–π^* transitions.[68] Moreover, Fig. S3(d) illustrates that the excitation wavelength maximizing the QY is approximately 360 nm, aligning with the n–π^* transition associated with the edge state. Taken together, these observations are consistent with the widely accepted view that excitation-dependent emission is primarily governed by surface states, rather than by quantum size effects.[70]

Finally, we compare the PL features for CDs-300 and CDs-480. As shown in Fig. 5(d), the emission wavelengths linked to defects in the carbon core, excited at less than 300 nm in CDs-300, remain relatively stable and exhibit a redshift of 39–45 nm compared with CDs-480. This redshift is attributed to the diverse types and quantities of defects present in the carbon core. Conversely, the excitation-dependent emission wavelength related to edge/surface states, excited above 300 nm in CDs-300, shows a similar trend to CDs-480, with slightly red-shifted peak wavelengths. This observation aligns with the notion that edge and surface states are minimally influenced by the size, shape, or quality of the carbon core. Furthermore, as shown in Fig. S3(e), the PL intensity in CDs-300 is significantly lower (approximately one-third) than that in CDs-480. Similarly, the QY of CDs-300 is diminished. The reduced PL intensity and QY in CDs-300 are believed to stem from an increase in non-radiative transitions induced by defects.

Conclusion

The rise in pyrolysis temperature caused a shift toward shorter emission wavelengths. Additionally, the FWHM of the CDs decreased by 13 nm, indicating enhanced color purity. Significantly, the QY improved by approximately threefold to approximately 30%, reaching a level comparable to that of naturally synthesized CDs using standard methods. These changes in emission wavelength, FWHM reduction, and QY enhancement were attributed to increased CD crystallinity. The PL mechanism seems similar to that of typical CDs synthesized from other chemical sources, as evidenced by the excitation-wavelength-dependent PL behavior common in previously reported CDs.[70] Our study offers novel insights into the synthesis of natural CDs with narrow FWHM and high QY.

Author contributions

K. Inoue: methodology, investigation, formal analysis, validation, writing of the original draft, and visualization. R. Suzuki: writing, review, editing, and supervision. Y. Kaneda and M. Tanimura: TEM observation and analysis. K. Shinozaki: support experimental and characterization. M. Tachibana: Supervision, funding acquisition, writing and review. All the authors contributed to the discussion.

Conflicts of interest

There are no conflicts to declare.

Data availability

The data supporting this article have been included as part of the supplementary information (SI). Supplementary information: Additional TEM images, PL spectra, characteristics of our CDs and previous natural CDs. See DOI: https://doi.org/10.1039/d5tc03150h.

Acknowledgements

Notes and references

1 M. Wang and S. Lu, *Matter*, 2022, **5**, 110–149.
2 X. Xu, R. Ray, Y. Gu, H. J. Ploehn, L. Gearheart, K. Raker and W. A. Scrivens, *J. Am. Chem. Soc.*, 2004, **126**, 12736–12737.
3 K. J. Mintz, Y. Zhou and R. M. Leblanc, *Nanoscale*, 2019, **11**, 4634–4652.
4 Y. Wang and A. Hu, *J. Mater. Chem. C*, 2014, **2**, 6921–6939.
5 Y. Yao, H. Zhang, K. Hu, G. Nie, Y. Yang, Y. Wang, X. Duanand and S. Wang, *J. Environ. Chem. Eng.*, 2022, **10**, 107336.
6 M. Jorns and D. Pappas, *Nanomaterials*, 2021, **11**, 1448.
7 M. J. Molaei, *Sol. Energy*, 2020, **196**, 549–566.
8 S. Zhu, Y. Song, X. Zhao, J. Shao, J. Zhang and B. Yang, *Nano Res.*, 2015, **8**, 355–381.
9 D. Pan, J. Zhang, Z. Li and M. Wu, *Adv. Mater.*, 2010, **22**, 734.
10 Y. Zhang, X. Liu, Y. Fan, X. Guo, L. Zhou, Y. Lv and J. Lin, *Nanoscale*, 2016, **8**, 15281.
11 T. T. Meiling, R. Schürmann, S. Vogel, K. Ebel, C. Nicolas, A. R. Milosavljević and I. Bald, *J. Phys. Chem. C*, 2018, **122**, 10217.
12 K. Jiang, S. Sun, L. Zhang, Y. Lu, A. Wu, C. Cai and H. Lin, *Angew. Chem., Int. Ed.*, 2015, **54**, 5360–5363.
13 X. Y. Meng, Y. Song, Q. Jing and H. G. Zhao, *J. Phys. Chem. Lett.*, 2023, **14**, 9176.

22838 | *J. Mater. Chem. C*, 2025, **13**, 22832–22840

This journal is © The Royal Society of Chemistry 2025

14 R. Das, R. Bandyopadhyay and P. Pramanik, *Mater. Today Chem.*, 2018, **8**, 96–109.

15 S. Chahal, N. Yousefi and N. Tufenkji, *ACS Sustainable Chem. Eng.*, 2020, **8**, 5566–5575.

16 B. Zhao, H. Ma, M. Zheng, K. Xu, C. Zou, S. Qu and Z. Tan, *Carbon Energy*, 2022, **4**, 88–114.

17 N. K. Khairol Anuar, H. L. Tan, Y. P. Lim, M. S. So'Aib and N. F. Abu Bakar, *Front. Energy Res.*, 2021, 9.

18 X. Wu, K. Abbas, Y. Yang, Z. Li, A. C. Tedesco and H. Bi, *Pharmaceuticals*, 2022, **15**, 487.

19 H. Li, J. Zheng, Y. Yang, L. Chen and X. Liu, *Adv. Opt. Mater.*, 2025, **13**, 2500148.

20 W.-K. Luo, L.-L. Zhang, Z.-Y. Yang, X.-H. Guo, Y. Wu, W. Zhang, J.-K. Luo, T. Tang and Y. Wang, *J. Nanobiotechnol.*, 2021, 19.

21 J. D. G. da Rocha, M. A. P. Cechinel, L. F. Rocha, H. G. Riella, N. Padoin and C. Soares, *Chem. Eng. J. Adv.*, 2024, **17**, 100583.

22 L. Zhu, Y. Yin, C.-F. Wang and S. Chen, *J. Mater. Chem. C*, 2013, **1**, 4925.

23 X. Tan, A. N. B. Romainor, S. F. Chin and S. M. Ng, *J. Anal. Appl. Pyrol.*, 2014, **105**, 157–165.

24 M. Chen, C. Liu, J. Zhai, Y. An, Y. Li, Y. Zheng, H. Tian, R. Shi, X. He and X. Lin, *RSC Adv.*, 2022, **12**, 18779–18783.

25 W. Matyjasik, K. Matus, O. Długosz, J. Pulit-Prociak and M. Banach, *ACS Omega*, 2025, **10**, 22529–22548.

26 A. Dager, A. Baliyan, S. Kurosu, T. Maekawa and M. Tachibana, *Sci. Rep.*, 2020, **10**, 12333.

27 N. Urushihara, T. Hirai, A. Dager, Y. Nakamura, Y. Nishi, K. Inoue, R. Suzuki, M. Tanimura, K. Shinozaki and M. Tachibana, *ACS Appl. Nano Mater.*, 2021, **4**, 12472–12480.

28 W. Li, Z. Yue, C. Wang, W. Zhang and G. Liu, *RSC Adv.*, 2013, **3**, 20662.

29 J. Liu, Y. Geng, D. Li, H. Yao, Z. Huo, Y. Li, K. Zhang, S. Zhu, H. Wei, W. Xu, J. Jiang and B. Yang, *Adv. Mater.*, 2020, **32**, 1906641.

30 S. Ren, B. Liu, M. Wang, G. Han, H. Zhao and Y. Zhang, *J. Mater. Chem. C*, 2022, **10**, 11338.

31 L. Tian, S. Yang, Y. Yang, J. Li, Y. Deng, S. Tian, P. He, G. Ding, X. Xie and Z. Wang, *RSC Adv.*, 2016, **6**, 82648–82653.

32 J. Xu, Y. Guo, T. Gong, K. Cui, L. Hou and C. Yuan, *Inorg. Chem. Commun.*, 2022, **145**, 110047.

33 W. Yang, H. Zhang, J. Lai, X. Peng, Y. Hu, W. Gu and L. Ye, *Carbon*, 2018, **128**, 78–85.

34 N. Basu and D. Mandal, *Carbon*, 2019, **144**, 500–508.

35 M. Tuerhong, Y. Xu and X.-B. Yin, *Chin. J. Anal. Chem.*, 2017, **45**, 139–150.

36 A. Nair, J. T. Haponiuk, S. Thomas and S. Gopi, *Biomed. Pharmacother.*, 2020, **132**, 110834.

37 G. Ayiloor Rajesh, V. L. John, A. Pookunnath Santhosh, A. Krishnan Nair Ambika and V. Thavarool Puthiyedath, *Part. Part. Syst. Charact.*, 2022, **39**, 2200017.

38 W. Li, Z. Zhang, B. Kong, S. Feng, J. Wang, L. Wang, J. Yang, F. Zhang, P. Wu and D. Zhao, *Angew. Chem., Int. Ed.*, 2013, **52**, 8151–8155.

39 S. Yang, J. Sun, X. Li, W. Zhou, Z. Wang, P. He, G. Ding, X. Xie, Z. Kang and M. Jiang, *J. Mater. Chem. A*, 2014, **2**, 8660.

40 S. Chaudhary, S. Kumar, B. Kaur and S. K. Mehta, *RSC Adv.*, 2016, **6**, 90526–90536.

41 Q. Ye, F. Yan, Y. Luo, Y. Wang, X. Zhou and L. Chen, *Spectrochim. Acta, Part A*, 2017, **173**, 854–862.

42 T. H. Chen and W. L. Tseng, *Anal. Chem.*, 2017, **89**, 11348–11356.

43 J. Chen, X. Zhang, Y. Zhang, W. Wang, S. Li, Y. Wang, M. Hu, L. Liu and H. Bi, *Langmuir*, 2017, **33**, 10259–10270.

44 R. Bandi, R. Dadigala, B. R. Gangapuram and V. Guttena, *J. Photochem. Photobiol., B*, 2018, **178**, 330–338.

45 N. Vasimalai, V. Vilas-Boas, J. Gallo, M. F. Cerqueira, M. Menéndez-Miranda, J. M. Costa-Fernández, L. Diéguez, B. Espiña and M. T. Fernandez-Argüelles, *Beilstein J. Nanotechnol.*, 2018, **9**, 530–544.

46 F. Arcudi, L. Dordevic and M. Prato, *Acc. Chem. Res.*, 2019, **52**, 2070–2079.

47 Y. Wan, M. Wang, K. Zhang, Q. Fu, M. Gao, L. Wang, Z. Xia and D. Gao, *Microchem. J.*, 2019, **148**, 385–396.

48 M. Shahshahanipour, B. Rezaei, A. A. Ensafi and Z. Etemadifar, *Mater. Sci. Eng., C*, 2019, **98**, 826–833.

49 T. Arumugham, M. Alagumuthu, R. G. Amimodu, S. Munusamy and S. K. Iyer, *Sustainable Mater. Technol.*, 2020, 23.

50 A. Boruah, M. Saikia, T. Das, R. L. Goswamee and B. K. Saikia, *J. Photochem. Photobiol., B*, 2020, **209**, 111940.

51 A. Tadesse, M. Hagos, D. Ramadevi, K. Basavaiah and N. Belachew, *ACS Omega*, 2020, **5**, 3889–3898.

52 W. L. Ang, C. A. L. B. Boon Mee, N. S. Sambudi, A. W. Mohammad, C. P. Leo, E. Mahmoudi, M. Ba-Abbad and A. Benamor, *Sci. Rep.*, 2020, **10**, 21199.

53 S. Ghosh, A. R. Gul, C. Y. Park, P. Xu, S. H. Baek, J. R. Bhamore, M. W. Kim, M. Lee, S. K. Kailasa and T. J. Park, *Microchem. J.*, 2021, **167**, 106272.

54 W. Li, N. Jiang, B. Wu, Y. Liu, L. Zhang and J. He, *Molecules*, 2021, **26**, 4994.

55 D. Ghosh Dastidar, P. Mukherjee, D. Ghosh and D. Banerjee, *Colloids Surf., A*, 2021, **611**, 125781.

56 P. Chauhan, S. Chaudhary and R. Kumar, *J. Clean. Prod.*, 2021, **279**, 123639.

57 M. Rizk, M. A. El-Alamin, D. Mohamed and S. Toubar, *Talanta Open*, 2022, **6**, 100127.

58 H. Shibata, M. Abe, K. Sato, K. Uwai, K. Tokuraku and T. Iimori, *Carbohydr. Polym. Technol. Appl.*, 2022, **3**, 100218.

59 N. Chaudhary, D. Verma, A. K. Yadav, J. G. Sharma and P. R. Solanki, *Talanta Open*, 2023, **8**, 100259.

60 S. Assariha, N. Alvandi, S. Rouhani and N. Esfandiari, *Luminescence*, 2023, **38**, 554–567.

61 B. I. Salman, M. A. Abdel-Lateef, E. Alzahrani, A. Al-Harrasi, A. E. Ibrahim, E. A. M. El-Shoura and Y. F. Hassan, *Luminescence*, 2024, **39**, e4801.

62 M. S. El-Semary, F. Belal, A. A. El-Emam, R. N. El-Shaheny and A. A. El-Masry, *Luminescence*, 2024, **39**, e4826.

63 S. R. Suseem, *RSC Adv.*, 2024, **14**, 17471–17479.

64 S. Wang, Z.-G. Chen, I. Cole and Q. Li, *Carbon*, 2015, **82**, 304–313.

65 H. K. Kohli and D. Parab, *Next Mater.*, 2025, **8**, 100527.

This journal is © The Royal Society of Chemistry 2025

J. Mater. Chem. C, 2025, **13**, 22832–22840 | **22839**

66 Z. Xu, W. Huang, C. Chen, W. Ye, B. Guo, J. Qiu, J. Zhuang, C. Hu, B. Lei, G. Hu and Y. Liu, *Mater. Today Chem.*, 2023, **27**, 101269.

67 Z. Gan, S. Xiong, X. Wu, T. Xu, X. Zhu, X. Gan, J. Guo, J. Shen, L. Sun and P. K. Chu, *Adv. Opt. Mater.*, 2013, **1**, 926–932.

68 Y. Chen, H. Lian, Y. Wei, X. He, Y. Chen, B. Wang, Q. Zeng and J. Lin, *Nanoscale*, 2018, **10**, 6734–6743.

69 G. Yang, C. Wu, X. Luo, X. Liu, Y. Gao, P. Wu, C. Cai and S. S. Saavedra, *J. Phys. Chem. C*, 2018, **122**, 6483–6492.

70 A. B. Siddique, S. M. Hossain, A. K. Pramanick and M. Ray, *Nanoscale*, 2021, **13**, 16662–16671.

71 Z. Gan, X. Wu and Y. Hao, *CrystEngComm*, 2014, **16**, 4981–4986.

22840 | *J. Mater. Chem. C*, 2025, **13**, 22832–22840

This journal is © The Royal Society of Chemistry 2025